SITE SELECTION AND LASER

SPECTROSCOPY OF

Nd^{3+} IN KYF_4

By

LIANG-CHIUN CHAO

Bachelor of Science

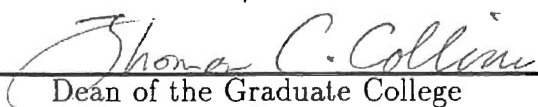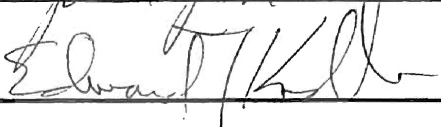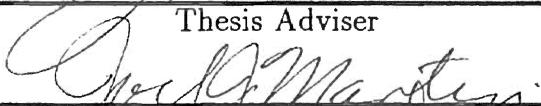Fu-Jen Catholic University

Taipei, Taiwan

1989

Submitted to the Faculty of the
Graduate College of the
Oklahoma State University
in partial fulfillment of
the requirements for
the Degree of
MASTER OF SCIENCE
July, 1993

SITE SELECTION AND LASER

SPECTROSCOPY OF

Nd^{3+} IN KYF_4

Thesis Approved:

_____

Thesis Adviser

_____

_____

_____

Dean of the Graduate College

ACKNOWLEDGMENTS

Dr. Roger J. Reeves, my advisor and also a good friend, is the one who makes this thesis possible. For the past sixteen months, he keeps giving me valuable suggestions and encouragement. I would like to express my deepest gratitude to him.

Special thanks go to Dr. Martin and Dr. Knobbe for kindly being my committee members. Thanks to Dr. Westhaus and all the faculty members in the Physics Department at Oklahoma State University.

My office mates Scott, Cindy, Roger, Bahman and Keith provided me a great environment for discussion where I always got valuable feedback.

I want to thank my parents for their understanding and support for these two years while I'm 10,000 miles away from home.

Finally I want to give thanks to Jesus. He is with me all the way.

TABLE OF CONTENTS

LIST OF TABLES

LIST OF FIGURES

CHAPTER I

INTRODUCTION

For laser crystals there are always some ions doped in the crystal as "activators" [1]. Those activators are responsible for absorbing and emitting photons. Rare earth ions, especially those trivalent ones, play a very important role in being those activators. All those trivalent ions have a xenon-like inner shell and N 4f electrons and their chemical properties are quite the same. One of the main feature that rare earth ions have is lanthanide contraction. Lanthanide contraction is a phenomenon that when the atomic number increases, those 4f electrons are being pulled closer and closer to the nucleus. That causes these 4f electrons being screened from their environment by 5d and 5s electrons. This also causes the 4f electrons to exhibit sharp absorption and emission lines when even being placed in a crystal [2]. Because of lanthanide contraction, the influence from the environment on those 4f electrons are small and they can be treated as perturbation.

When looking for a suitable laser crystals, one is always looking for low nonlinear effect, high optical damage resistance, wide range of transparency and good photo chemical stability [3]. Currently there are two major types of laser crystals, fluoride compounds and oxide compounds. Also there is a small portion of bromide and chloride compounds [1]. Among them the fluoride compounds attract more attention recently because of their physical and chemical properties [3]. One of the fluoride compound, KY-YF$_3$ host, is noticeable in which KY$_3$F$_{10}$ is already known as a laser material, K$_2$YF$_5$, a possible one and KYF$_4$, also exhibits promising characteristics at 1047nm, [3],[4],[5].

1

Summary

The aim of this thesis is to report the experimental results of site selection spectroscopy, room temperature energy levels and up-conversion properties of Nd^{3+} in KYF_4. Chapter II deals with theoretical background for predicting the energy levels by using matrix operator method. Chapter III describes experiment set up and Chapter IV presents results of this experiment. 17 out of 41 energy levels of A B site are determined under room temperature. At 10K, two sites have been observed and each site has three subsites while at room temperature there are only two sites are left. Up-conversion is obtained by pumping the ion from the ground state to R. We observed blue emission from 300nm to 500nm which is probably the transition from $^4D_{3/2}$ to $^4I_{9/2}, ^4I_{11/2}, ^4I_{13/2}, ^4I_{15/2}$. Luminescence lifetimes are measured for different sites and different transitions. Chapter V is summary and future work.

CHAPTER II

THEORY REVIEW

The total Hamiltonian of an atom in a crystal can be given as

$$H = H_0 + H_{ele} + H_{so} + H_{cf} \qquad (1)$$

where the first term describes the effect of coulomb potential, the second term describes the interaction between electron pairs, the third term is spin-orbit interaction and the last one is the interaction between electrons and their environment. The first two terms can be treated by the central field approximation, then use the eigenvalues obtained by the central field approximation, the last two terms can be treated as perturbations.

Central Field Approximation

First of all, consider the first two terms in Eq. (1). The non-relativistic Hamiltonian for a free atom with N electrons can be written as

$$H = -\frac{\hbar^2}{2m} \sum_{i=1}^{N} \nabla_i^2 - \sum_{i=1}^{N} \frac{Ze^2}{r_i} + \sum_{i<j}^{N} \frac{e^2}{r_{ij}} \qquad (2)$$

The first term on the right hand side is the summation of the kinetic energy of each individual electron. The second term is the total coulombic potential energy due to the interaction between electrons and nucleus. The third term describes the interaction between electron pairs. This equation can only be solved exactly for N = 1. For N > 1, the central field approximation becomes necessary. The basic idea of central field approximation is assuming that each electron moves independent of each other and it feels a spherical symmetric coulombic potential $-\frac{U(r)}{e}$, which is

caused by the nucleus and other electrons. Following this assumption the central field Hamiltonian, [6] , can be written as

$$H_c = \sum_{i=1}^{N} \left[-\frac{\hbar^2}{2m} \nabla_i^2 + U(r_i) \right] \tag{3}$$

and the difference between Eq. (2) and Eq. (3) is

$$H - H_c = V = \sum_{i=1}^{N} \left[-\frac{Ze^2}{r_i} - U(r_i) \right] + \sum_{i<j}^{N} \frac{e^2}{r_{ij}} \tag{4}$$

The solution to the central field Schrödinger equation:

$$\sum_{i=1}^{N} \left[-\frac{\hbar^2}{2m} \nabla_i^2 + U(r_i) \right] \Psi = E_c \Psi \tag{5}$$

is:

$$\Psi = \sum_{i=1}^{N} \varphi_i(a^i) \qquad \text{and} \qquad E_{cf} = \sum_{i=1}^{N} E_i \tag{6}$$

where $\varphi_i(a^i)$ is the eigenfunction of the central field Hamiltonian. (a^i) is a set of quantum numbers. According to the assumption that each electron moves *independently* so we can treat this problem as hydrogenic. The solution to Eq. (5) can be written as, [6]:

$$\varphi(a_i) = r^{-1} R_{nl}(r) Y_{lm_l}(\theta, \phi) \tag{7}$$

where $R_{nl}(r)$ is the radial part, depends on the central field potential U(r), $Y_{lm_l}(\theta, \phi)$ is the spherical harmonic functions:

$$Y_{lm_l}(\theta, \phi) = (-1)^m \left[\frac{(2l+1)(l-\mid m \mid)!}{4\pi(l+\mid m \mid)!} \right]^{\frac{1}{2}} P_l^m(\cos \theta) e^{im\phi} \tag{8}$$

and

$$P_l^m(\omega) = \frac{(1-\omega^2)^{\frac{m}{2}}}{2^l l!} \frac{d^{m+1}}{d\omega^{m+1}} (\omega^2 - 1)^l \tag{9}$$

is the associated Legendre polynomials with ω equals to $\cos\theta$, θ is the angle between the position vector of the electron and the z-axis.

Eq. (7) does not contain m_s, the electron spin quantum number which could be $\pm\frac{1}{2}$. Follow Wybourne's work, another coordinate σ, is added into the solution:

$$\varphi(nlm_lm_s) = \delta(m_s,\sigma)r^{-1}R_{nl}(r)Y_{lm_l}(\theta,\phi) \tag{10}$$

Besides, the total wave function needs to be anti symmetric in order to satisfy Pauli exclusion principle, the total wave function can be written:

$$\Psi = \frac{1}{\sqrt{N|}} \begin{vmatrix} \varphi_1(\alpha^1) & \varphi_2(\alpha^1) & \cdots & \varphi_N(\alpha^1) \\ \varphi_1(\alpha^2) & \varphi_2(\alpha^2) & \cdots & \varphi_N(\alpha^2) \\ \vdots & \vdots & \ddots & \vdots \\ \varphi_1(\alpha^N) & \varphi_2(\alpha^N) & \cdots & \varphi_N(\alpha^1) \end{vmatrix} \tag{11}$$

This is the solution to Eq. (5) which is the central field Hamiltonian.

<center>Electrostatic Interaction: $\frac{e^2}{r_{ij}}$</center>

Before we go any further, we need to change the notation. According to Russel-Saunders coupling scheme, each electron's angular momentum are coupled to form a resultant angular momentum that is given by:

$$\overrightarrow{L} = \sum_{i=1}^{N} \overrightarrow{l_i} \tag{12}$$

and also for spin-momentum:

$$\overrightarrow{S} = \sum_{i=1}^{N} \overrightarrow{s_i} \tag{13}$$

and the total spin, angular momentum coupled to form a total angular momentum $\overrightarrow{J}$ for which

$$|L - S| \le J \le |S + L| \tag{14}$$

Also it's possible that there are more than one term that have the same $\overrightarrow{L}$, $\overrightarrow{S}$ values, in adding another quantum number τ can tell the difference. As a result, the eigenvectors can be written as

$$| \Psi >=| \tau SLJM > \tag{15}$$

and the perturbation matrix becomes

$$\left\langle \tau SLJM \left| H_p \right| \tau' S' L' J' M' \right\rangle \tag{16}$$

According to Wybourne 1965,[6], the first term in Eq. (4) is radial and is the same for all the levels in the same configuration so that term has no contribution. Here Dieke [2] explained that a given configuration means quantum number n,l are given but m_l, m_s can be any one of the allowed states which implies that the radius of the electron orbit is fixed but it's orientation and spin orientation can be any one of the allowed directions. For the second term is Eq. (4), only electrons in the partially filled states need to be consider because for electrons in the completely filled states, the total result will average to zero. The second term is small and can be treated as a perturbation to the central field:

$$\left\langle \tau SLJM \left| \sum_{i<j} \frac{e^2}{r_{ij}} \right| \tau' S' L' J' M' \right\rangle \tag{17}$$

The $\frac{e^2}{r_{ij}}$ can be expanded by Legendre polynomials:

$$\frac{1}{|r_{ij}|} = \sum_{i<j} \frac{r_<^k}{r_>^{k+1}} P_k(\cos \omega_{ij}) \tag{18}$$

ω_{ij} is the angle between $\vec{r_<}, \vec{r_>}$ and $|r_{ij}| = \left| \vec{r_<} - \vec{r_>} \right|$. The Legendre polynomial can also be expanded by spherical harmonic functions:

$$P_k(\cos \omega_{ij}) = \frac{4\pi}{2k+1} \sum_q Y_{kq}^*(\theta_i, \phi_j) Y_{kq}(\theta_i, \phi_j)$$

$$= \sum_q (-1)^q (\mathbf{C}_{-q}^{(k)})_i (\mathbf{C}_q^{(k)})_j$$

$$= \left(\mathbf{C}_i^{(k)} \cdot \mathbf{C}_j^{(k)} \right) \tag{19}$$

here $\mathbf{C}_q^{(k)}$ is:

$$\mathbf{C}_q^{(k)} = \left(\frac{4\pi}{2k+1}\right)^{\frac{1}{2}} Y_{kq} \tag{20}$$

So Eq. (17) becomes:

$$\sum_k e^2 \left\langle \tau S L \left| \sum_{i<j} \frac{r_<^k}{r_>^{k+1}} \left(\mathbf{C}_i^{(k)} \cdot \mathbf{C}_j^{(k)}\right) \right| \tau' S' L' \right\rangle \tag{21}$$

There are two parts in Eq. (21), radial and angular parts. The former one can be calculated by Slater's integral and the latter one can be calculated by Racah's tensor operator method [7],[8],[9]. All of those terms for $4f^n$ electrons are tabulated by Nielson and Koster [10]. The final results, according to Wybourne, can be written as:

$$E = \sum_{k=0}^{6} f_k F^k(nf, nf) = \sum_{k=0}^{6} f^k F_k(nf, nf) \tag{22}$$

k is even and f_k is the angular part. The matrix element then becomes:

$$E = \sum_{k=0}^{3} e_k E^k \tag{23}$$

for which,

$$
\begin{aligned}
e_0 &= f^0 = n(n-1) \\
e_1 &= \frac{9f^0}{7} + \frac{f^2}{42} + \frac{f^4}{77} + \frac{f^6}{462} \\
e_2 &= \frac{143f^2}{42} - \frac{130f^4}{77} + \frac{35f^6}{462} \\
e_3 &= \frac{11f^2}{42} + \frac{4f^4}{77} - \frac{7f^6}{462}
\end{aligned}
\tag{24}
$$

and

$$
\begin{aligned}
E^0 &= F_0 - 10F_2 - 33F_4 - 286F_6 \\
E^1 &= \frac{70F_2 + 231F_4 + 202F_6}{9} \\
E^2 &= \frac{F_2 - 3F_4 + 7F_6}{9} \\
E^3 &= \frac{5F_2 + 6F_4 - 91F_6}{9}
\end{aligned}
\tag{25}
$$

The electrostatic energy is represented in Eq. (23) as a linear combination of those terms from Eq. (24). The coefficients e_k can be found from Nielson and Koster's

book [10]. The energy split caused by electrostatic interaction is tabulated in Table I.

<div align="center">Spin-Orbit Interaction: H$_{so}$</div>

The Hamiltonian for spin-orbit interaction can be written as:

$$H_{so} = \sum_{i=1}^{N} \zeta(r_i)(\mathbf{s}_i \cdot \mathbf{l}_i) \qquad (26)$$

where

$$\zeta(r_i) = \frac{\hbar^2}{2m^2c^2r_i}\frac{dU(r_i)}{dr_i} \qquad (27)$$

U(r$_i$) is the one used in central field approximation in Eq. (3). Here, again the spin-orbit interaction can be treated as a perturbation by using Racah's tensor operator. According to Wyburne [6] we have:

$$\left\langle l^N \alpha SLJM \left| \zeta_{nl} \sum_{i=1}^{N} (\mathbf{s}_i \cdot \mathbf{l}_i) \right| l^N \alpha' S' L' J' M' \right\rangle = \zeta_{nl}(-1)^{J+L+S'} \left\{ \begin{array}{ccc} L & L' & 1 \\ S' & S & J \end{array} \right\}$$

$$\times [l(l+1)(2l+1)]^{\frac{1}{2}} \left\langle l^N \alpha SL \left\| \mathbf{V}^{(11)} \right\| l^N \alpha' S' L' \right\rangle$$

$$(28)$$

The middle term $\left\{ \begin{array}{ccc} L & L' & 1 \\ S' & S & J \end{array} \right\}$ is a 3-j symbol and can be derived from Clebsch-Gordon coefficient of Condon and Shortley [11] by :

$$\left\{ \begin{array}{ccc} j_1 & j_2 & j_3 \\ m_1 & m_2 & m_3 \end{array} \right\} = (-1)^{j_1-j_2-m_3} ([j_3])^{-\frac{1}{2}} \left\langle j_1 m_1 j_2 m_2 \mid j_1 j_2 j_3 - m_3 \right\rangle \qquad (29)$$

The last term in Eq. (28) $\mathbf{V}^{(11)}$, is tabulated in Nielson & Koster's book [10].

The spin-orbit interaction can be approximately evaluated by noting that the energy shift equals to :

$$\Delta E = \alpha \left[J(J+1) - L(L+1) - S(S+1) \right] \qquad (30)$$

where α is the coupling constant.

TABLE I

ELECTROSTATIC ENERGY OF 4f^3 ELECTRONS

^4S	0
^4D	$33E_3$
^4F	0
^4G	$12E_3$
^2P	$3E_1 - 11E_3$
$^2D_1$	$3E_1 - 858E_2/7 - 33E_3/7$
$^2D_2$	$3E_1 + 1131E_2/7 + 12E_3/7$
$^2F_1$	$9E_1$
$^2F_2$	$3E_1 + 195E_2 + 33E3$
$^2G_1$	$3E_1 + 195E_2 + 33E_3$
$^2D_1$	$3E_1 + 1131E_2/7 + 12E_3/7$
$^2G_2$	$3E_1 - 1683E_2/7 + 187E_3/7$
$^2H_1$	$3E_1 + 3E_3$
$^2H_2$	$3E_1 + 21E_2 - 24E_3$
^2I	$3E_1 - 30E_2 + 3E_3$
^2K	$3E_1 - 135E_2 - 11E_3$
^2L	$3E_1 + 105E_2 - 3E_3$

Ref. [10]

Crystal Field Interaction: H_{cf}

The last thing needs to talk about is crystal field interaction. For a free ion, spherical symmetry exists. When this ion is being placed in a crystal, this symmetry no longer holds because of the electric field caused by it's surrounding environment. This electric field also breaks the (2J+1) fold degeneracy. However, because of the lanthanide contraction, this influence can be regarded as a perturbation to the free ion Hamiltonian. As a result we can write:

$$H = H_f + H_{cf}$$

where H_f is the free ion Hamiltonian and H_{cf} is the crystal field Hamiltonian. By assuming that the free ion Hamiltonian as known, we can expand the crystal field Hamiltonian by a series of spherical harmonic operators because the free ion Hamiltonian's eigenfunction possesses spherical symmetry, [6]. So:

$$H_{cf} = \sum_{k,q,i} B_q^k (\mathbf{C}_q^k)_i$$

where $\mathbf{C}_q^{k'}s$ are tensor operators and i goes for all those electrons that involved.

For f^N configuration this perturbation can be written as:

$$\left(f^N \alpha SLJJ_z \left| H_{cf} \right| f^N \alpha' SL'J'J'_z \right) = \sum_{k,q} B_q^k \left\langle f^N \alpha SLJJ_z \left| \mathbf{U}_q^* \right| f^N \alpha' SL'J'J'_Z \right\rangle$$
$$\left\langle f \left\| \mathbf{C}^{(k)} \right\| f \right\rangle$$

Those coefficients has been tabulated by Judd [12]and Nielson & Koster [10]. Crystal field calculation is difficult in some sense because it requires a complete knowledge of the symmetry properties of the ion site that one is interested in. Actually, theoretical result doesn't meet with experiment result. The main reason is because of the omission of relativistic effect and three body interaction. Theoretical calculated energy levels must be adjusted to fit experiment result by finding a suitable values of F_2 and ζ to find the eigenfunction. Fig. (1) shows part of the energy levels due to electrostatic, spin-orbit and crystal field splitting for $4f^3$ electrons. Their magnitudes are $\sim 10,000 cm^{-1}, 1,000 cm^{-1}$ and $100 cm^{-1}$ respectively.
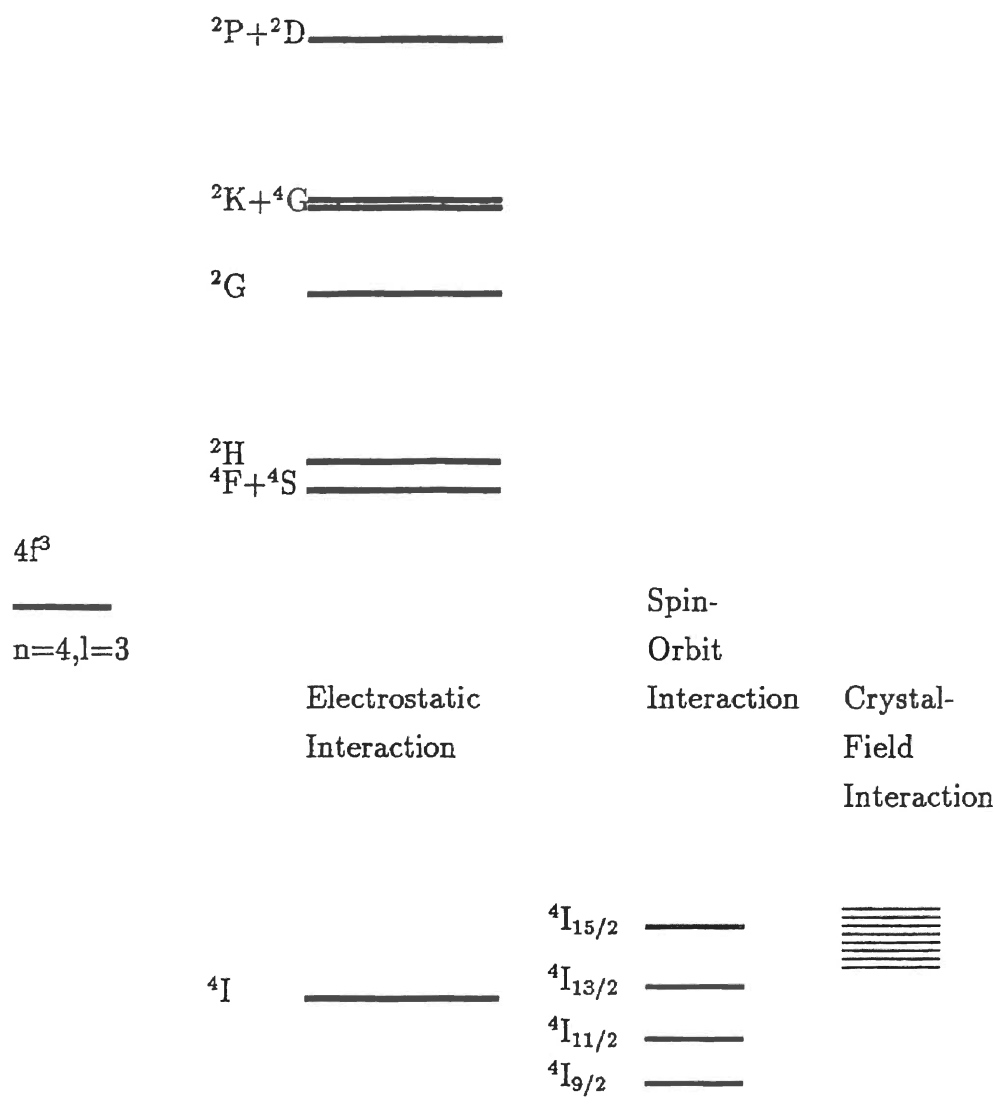
$^2P+^2D$ _____

$^2K+^4G$ ══════════

^2G _____

^2H ════════════
$^4F+^4S$ ════════════

$4f^3$

_____

n=4,l=3

Electrostatic
Interaction

Spin-
Orbit
Interaction

Crystal-
Field
Interaction

$^4I_{15/2}$ _____

^4I _____ $^4I_{13/2}$ _____

$^4I_{11/2}$ _____

$^4I_{9/2}$ _____

Figure 1. Energy Levels of $4f^3$ Electrons

CHAPTER III

EXPERIMENT

Crystal Preparation

The KYF_4 crystal was grown by Bruce H. T. CHAI , CREOL, University of Central Florida. This crystal was grown along the c-axis by using top-seeded solution growth technique and has a melting point of $1060°C$. The concentration of Nd ions is 2% which is determined by measuring the distribution coefficient of $Nd^{3+}(=0.6)$. The KYF_4 crystal belongs to space group $P3_1 12$ (D_3^3). It's lattice parameters are a=14.101A , c=10.087 A. The crystal structure has been investigated by Aleonard et al. [13] and it's crystal structure is shown on Fig. 2. Their result shows that this crystal has a hexagonal unit cell which contains three layers of atoms follow the 'abc' sequence. Each layer has twelve cation positions. Four of them are occupied by Y^{3+}. The other four are occupied by Y^{3+} or K^+ with a statistical ration of 1:2. The last four are also occupied by Y^{3+} or K^+ but with a ration of 1:5. This crystal has no center of inversion.

Experimental Set Up

Figure 3 shows the set up of this experiment. The dye laser used is a Molectron DL II tunable dye laser which has a line-width of 0.03nm at 400nm to 600nm and 0.12nm at 700nm to 850nm. The dye laser was previously pumped by a Molectron UV14 pulsed nitrogen laser with a repetition rate of 13Hz. This nitrogen laser works very well for visible light range but when it comes to infrared, it becomes very difficult to make IR dyes lase. As a result, we changed the nitrogen laser to a Continuum Surelite II Nd:YAG laser which has a repetition rate of 10Hz. This
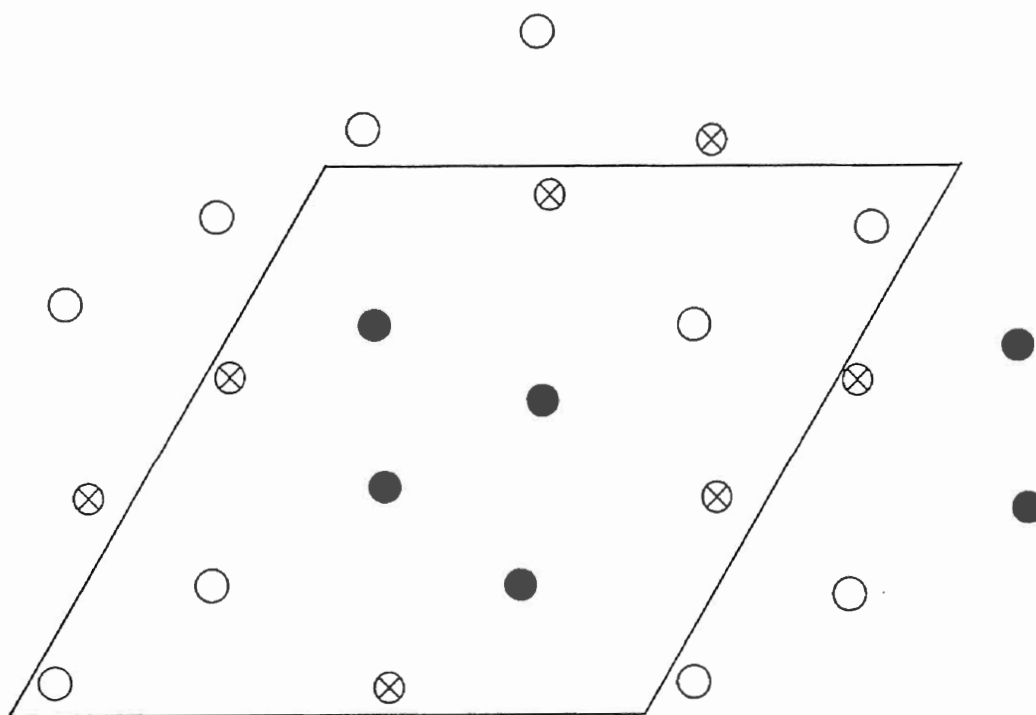
Figure 2. Crystal Structure of KYF_4, Projection (001), 1/3 Plane
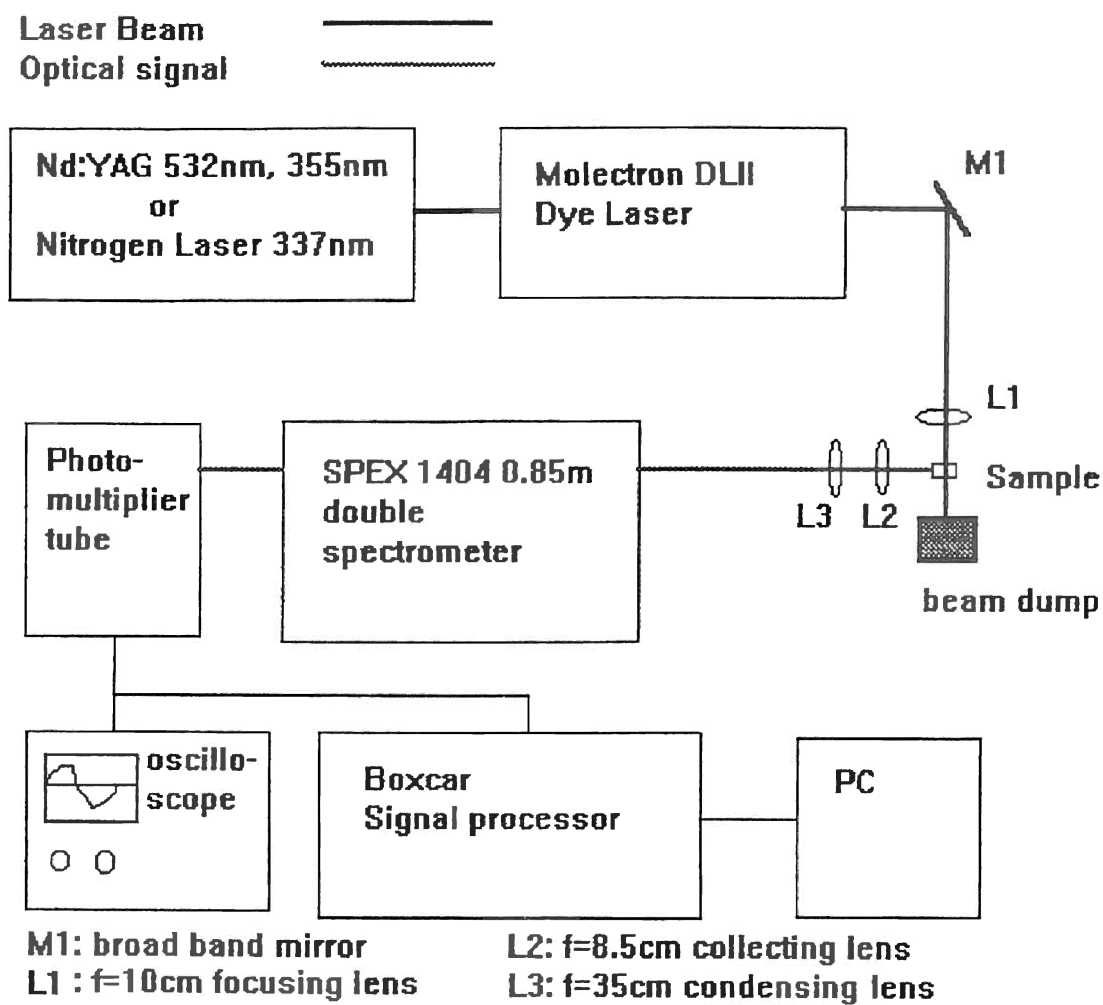
Ref. [11]

Figure 3. Experimental Set Up

Nd:YAG laser, equipped with a second and third harmonic generators, enables us to obtain tunable lasing range from 400nm to 880nm.

For Nd:YAG 532nm pumping, before the laser beam goes into the dye laser, it is directed to go through a variable power attenuator and being reflected off by a 532nm dichroic and a 532nm High Reflector (HR) in order to get rid of 1064nm which is the original lasing wavelength of Nd:YAG. For 355nm pumping, the variable power attenuator is unnecessary because the power is low enough but a separation process is still necessary. Being without a 355nm dichroic, we use three 355nm HR to 'filter' out both 1064nm and 532nm.

In Fig. 3, M1 is a broad band mirror, L1 is a silicon glass 2in focusing lens used to focus the laser beam down to the crystal. L2, L3 are both CaF_2 lenses which are transparent from 300nm to $1.2\mu m$. Sample is positioned right at the focal point of L2. L3 is positioned at 35cm away from the slit of the spectrometer in order to match the f number of the spectrometer, f/6.9. The slits at the spectrometer are $100\mu m/2mm/2mm/100\mu m$. The SPEX 1404 0.85m double spectrometer has a grating of 1200gr/mm blazes at 800nm, installed. It's dispersion and maximum resolution are 0.48nm/mm and 0.05nm respectively, operated at a step mode rather than a continuous mode.

The resolution of the spectrometer depends on the width of the slits. If the slits are $100\mu m$, then the resolution is:

$$\text{resolution} = 100\mu m. \times 0.48nm/mm \cong 0.05nm$$

A rule of thumb is that each peak should has at least five points, so the step interval of the spectrometer should be set to be 0.01nm that it can tell the difference of two peaks if their peaks are 0.05nm away from each other. According to this calculation it shows that in order to have good resolution, the scan rate should be slow and the slits should be as small as possible. But in narrowing the slit, it also decreases the signal strength quadratically. An optimum value for the slit width and scan rate should be found for each individual case.

Two photo multiplier tubes are used, one for visable range and the other for infrared range. The former one is cooled by water and it's active range is from 280nm to 900nm. The latter one is cooled to -50°C by liquid nitrogen and is active from 800nm to 1.2μm. The signal is processed by an EG&G Model 4402 signal processor and averaged by an EG&G Model 4420 boxcar. The signal is monitored by a oscilloscope and final results are saved in a computer. The spectrometer and the photo multiplier tube are controlled by the same computer. Both the boxcar and the oscilloscope are triggered by the YAG laser (or Nitrogen laser).

Transmission Spectra

The transmission spectra at 10K or Room Temperature are taken by using CARY 2400 spectrometer and SPEX 1404 spectrometer. When using CARY 2400, the sample is installed in a CTI-CRYOGENICS cryostat which utilizes compressed liquid helium to lower the temperature to 10K. Fig. 4 shows the transmission spectrum at room temperature without polarization.

Transmission spectra on the SPEX 1404 are taken by using a broad band quartz halogen lamp. Low temperature (10K) is also obtained by using an APD Model 1R02A cryostat.

10K Emission Spectra

For 10K emission spectra, the laser beam is directed to be perpendicular to the $\overrightarrow{C}$ axis with the polarization direction parallel to the $\overrightarrow{C}$ axis of the crystal. The luminescence is collected parallel to $\overrightarrow{C}$ axis. The dye laser is pumped by a Molectron pulsed nitrogen laser with an average output power of 20 mW for Rhodamine 6-G and 10mW for Stilbene 420. The dye laser has a line width of 0.03nm. Dyes used are Rhodamine 6-G and Stilbene 420 in order to excite the atom from the ground state $^4I_{9/2}$ to $^2G_{7/2} + ^4G_{5/2}$ and to $^2P_{1/2}$ respectively.

Dieke [2] shows that the transition from $^4I_{9/2}$ to $^2P_{1/2}$ is about 23000cm^{-1} which equals to 434.8nm for Nd^{3+} in LaCl$_3$. In our transmission spectra, Fig. 5,
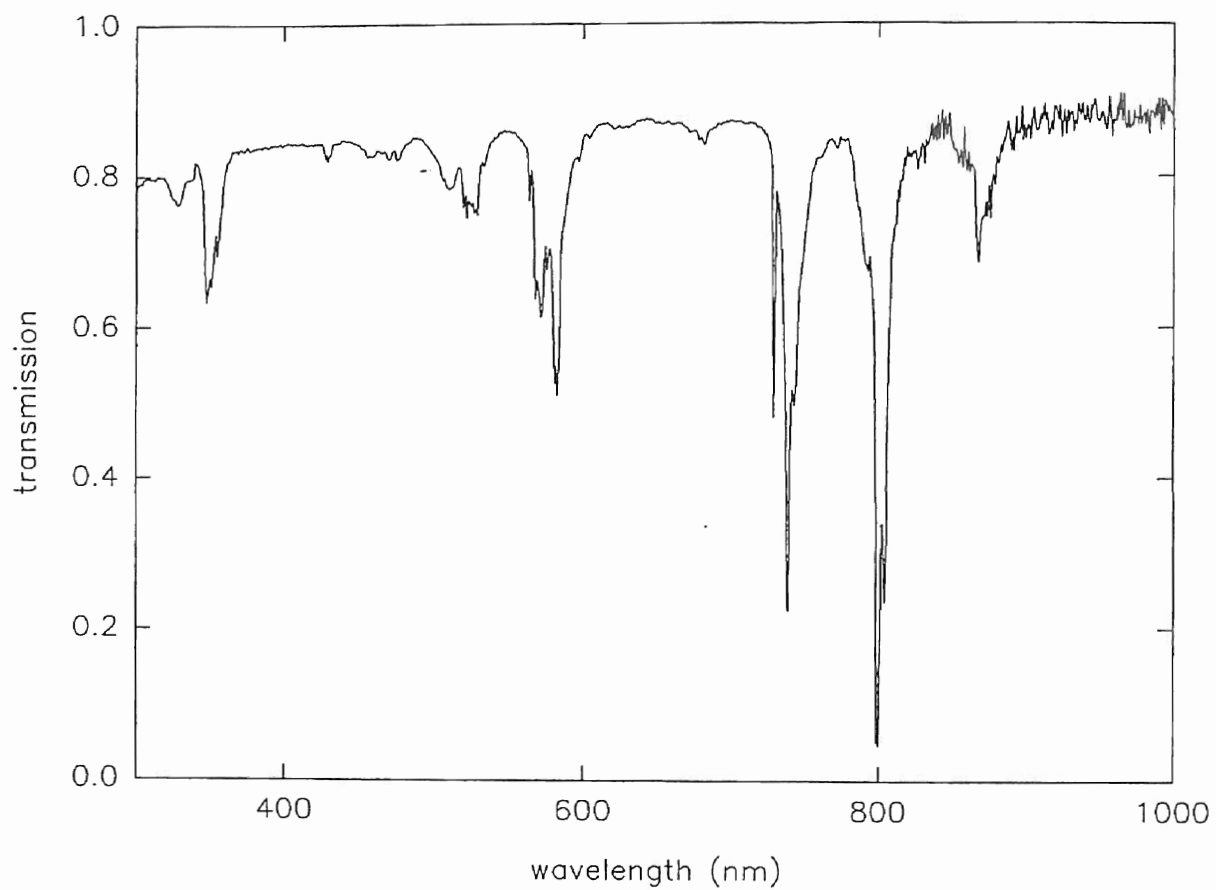
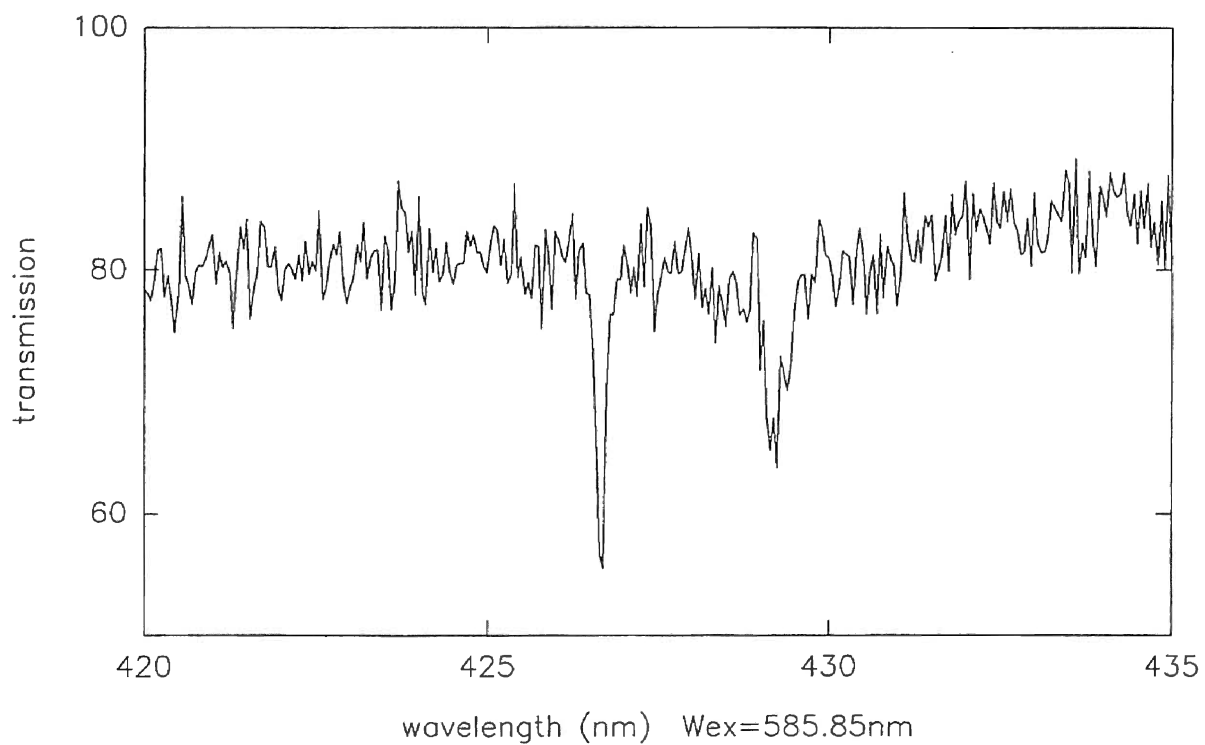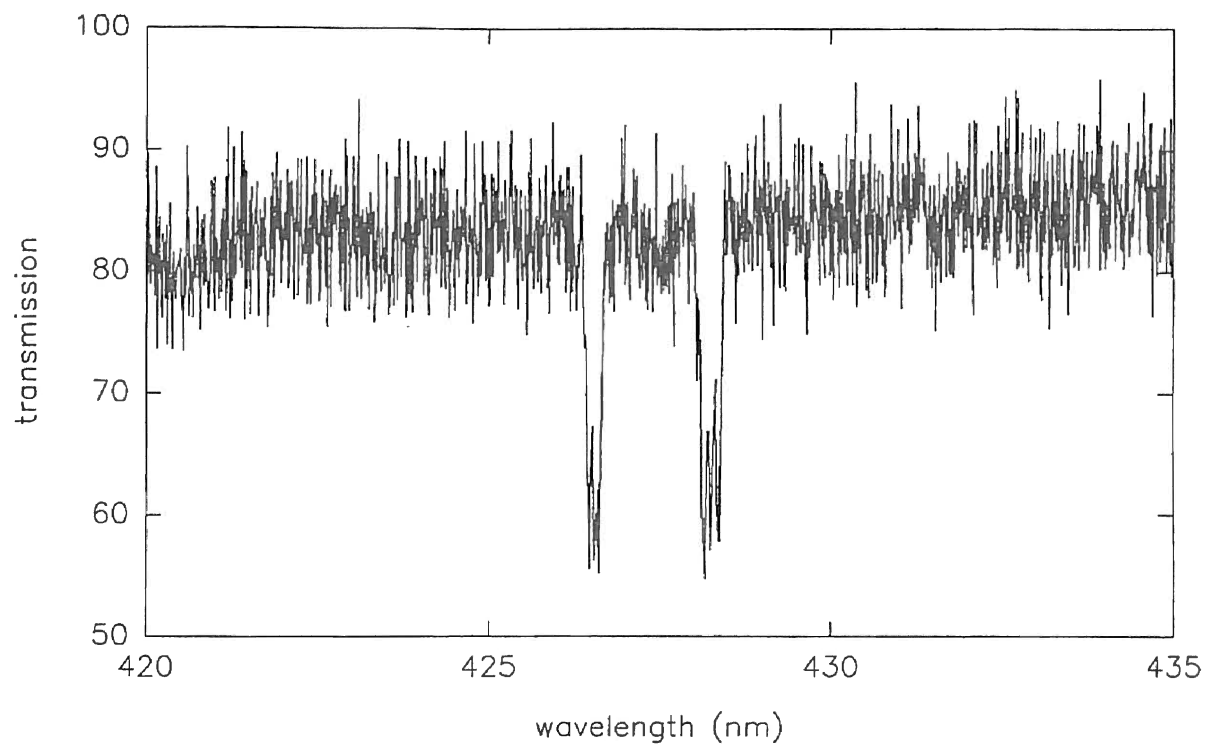Figure 4. Transmission spectrum of Nd^{3+}: KYF_4 No polarization with K perpendicular to C axis T=300K

Figure 5. Transmission spectra of Nd^{3+}:KYF_4 at 9.5K (upper one) and 300K (lower one) for the transition from $^4I_{9/2} \rightarrow {}^2P_{1/2}$

from 420nm to 440nm, we found two peaks and we believe that's the transition from $^4I_{9/2}$ to $^2P_{1/2}$. For $^2P_{1/2}$ there should be only one peak but here we have two which means that there are two main Stark components. We assign the 426.60nm as A site and 428.20nm as B site just because of their position. Site selection spectra are obtained by positioning the dye laser at one of these peaks and observing the fluorescence of the transition from $^4F_{3/2}$ to $^2I_{11/2}$. From the first rough spectrum, we position the monochrometer at each one of the emission lines and tune the dye laser to optimize the fluorescence signal and take the fluorescence spectrum again. Then, treat the other peaks in $^2P_{1/2}$ the same way. The reason for why we use this method is because for different sites there should have different emission spectra, by measuring those spectra we can determine how many sites there are. The results are shown in Chapter III. The same technique is also used for R-6G pumping and Room Temperature site selection spectra.

Room Temperature Energy Levels

At room temperature there are still two peaks in the transmission spectrum. The A site and B site are now at 427.1nm and 429.1nm respectively (see Fig. 5). We use the method mentioned previously and pump the atom from $^4I_{9/2}$ ground state to $^2P_{1/2}$. We found that there are only two different types of emission spectra left. From those two different emission spectra (Fig. 9) it shows that peak 855.5nm belongs to A site and peak 876.0nm belongs to B site while 868.0nm belongs to both of them. This phenomenon suggests that we should turn the spectrometer to each one of them and scan the dye laser over the energy levels' range. By comparing the relative intensity change when the spectrometer moves from site A to site B we can determine the energy levels of site A and B because for emissions from the same site, they should always have the same relative intensity. Based on this, we position the spectrometer at 854.3nm -A; 856.6nm A; 858.8nm A-; 874.5nm -B; 876.6nm B; 878.4nm B-, with a 100μm slit and finally, 868.0nm A+B, with both slits open, run the spectrometer at time scan mode and use a step motor to control the dye laser at the same time. The dial reading on the dye laser is recorded and

dye laser's wavelength is also measured by the spectrometer in order to convert the time domain to wavelength domain. The final results are tabulated in Table II.

By comparing the relative intensities in the time-domain spectra we determined the energy levels from 400nm to 890nm. For Nd: YAG 532nm pumped dye laser, those dyes used are: LDS867, LDS821, LDS765, LDS751, LDS698, LDS688, Rhodamine 640, Rhodamine 610, Rhodamine 590. For Nd:YAG 355nm pumped dye laser, we use Coumarin 500, LD466, Coumarin 460, Coumarin 440. For nitrogen laser pumped dye laser we use Stilbene 420, Rhodamine 640.

The major difficult encountered here is obtaining lasing for the LDS series dyes. As the wavelength increases, the difficulty for obtaining lasing also increases and the output power is always very low.

Up-Conversion

At the beginning, we tried to pump the atoms from the ground state $^4I_{9/2}$ to $^4F_{9/2}$ and from $^4F_{9/2}$ to M by using two dye lasers. This try did not success and we think synchronization may be the reason bcause for the two pulse lasers, there was a jittering of about 5μsec and we couldn't get them closer. Then we used a 20mW CW He-Ne laser and a dye laser. The transmission peak of the energy level M rises from 323nm dies at 331nm and has a peak at 328nm. The dye used is LD688 and LDS698. By position the dye laser at 679.86nm, 682.36nm, 684.86nm, 687.36nm, 689.86nm, 692.34nm, 694.86nm, plus the He-Ne laser, then we are pumping the atoms from the gound state to 327.78nm, 328.36nm,328.93nm,329.51nm, 330.08nm,330.65nm,331.22nm. We scan the monochrometer from 300nm to 500nm. The result shows that there are something, but they are really small and unsteady.

Finally we change the dye to R-6G, that is pumping the energy levels of $^2G_{7/2}$ $+\ ^4G_{5/2}$ and we do obtain emissions at around 350nm, 380nm, 410nm and 445nm. To double check those emission lines, we take the spectrum again by blocking the

grating on the dye laser or by installing a filter in front of the monochrometer. The results show that they are really blue emission.

TABLE II

ENERGY LEVELS OF Nd^{3+}:KYF_4
AT ROOM TEMPERATURE

energy levels	Site A (cm^{-1})	Site B (cm^{-1})
$^2P_{1/2}$	23413	23272
$^2G_{11/2}$	21938	21920
	21920	21848
	21882	21769
	21713	21700
	21645	21653
	21502	21502
$^2D_{3/2}$	21317	21287
	21307	21267
$^4G_{9/2}$	21049	21042
	21037	21030
	21027	20991
	20991	20970
	20931	20953
$^2G_{9/2}$	19768	19743
	19755	19637
	19724	19566
	19671	19537
	19611	19521
$^4G_{7/2}$	19233	19181
	19086	19138
	19052	18951
	18976	18897

TABLE II (Continued)

energy levels	Site A (cm^{-1})	Site B (cm^{-1})
$^2G_{7/2}$	17735	17609
$+$	17611	17562
$^4G_{5/2}$	17520	17461
	17492	17245
	17352	17147
	17225	17139
	17121	17121
$^2H_{11/2}$	16529	16145
	16298	16119
	16157	16033
	16108	
	16088	
	16045	
$^4F_{9/2}$	14879	14756
	14839	14696
	14737	14671
	14681	14662
	14636	14649
$^4S_{3/2}$	13712	13705
$+$	13696	13584
$^4F_{7/2}$	13658	13543
	13598	13515
	13538	13457
	13527	13441
$^2H_{9/2}$		
$+$		
$^4F_{5/2}$		12603

TABLE II (Continued)

energy levels	Site A (cm^{-1})	Site B (cm^{-1})
	12535	12528
	12512	12497
	12483	12471
	12449	12449
	12407	12431
$^4F_{3/2}$	11694	11511
	11525	11465

CHAPTER IV

EXPERIMENTAL RESULTS

Site Selection Spectra

As a result, we find six different emission spectra when pumping the atoms from the ground state to the $^2P_{1/2}$ state. Fig. 5 shows the result of those six different emission spectra at 10K. From those emission spectra we can identify two main sites. Each site has three subsites. The maximum wavelength shift for B subsites is 1049.40 from B2 shifts 0.7nm to 1048.70 at B3. The maximum wavelength shift for A subsites is 1039.90nm from A2 shifts 0.55nm to 1039.35nm at A1. The assignment of A1, A2, A3, B1,..., depends on the excitation wavelength. B1, B2, B3 has a pumping wavelength equals to 428.6nm, 428.5nm and 428.425nm. A1, A2, A3 has a pumping wavelength of 426.90nm, 426.80nm and 426.70nm. They are quite close but they are different because the emission spectra are different. The transmission spectrum of the transition $^4I_{9/2}$ to $^2P_{1/2}$ (see Fig. 4) also suggests that it's a multi-subsite construction.

At 10K, when pumping A site, we can also see B site transmission. In Fig. 6, 1040nm and 1063nm belong to A while peaks around 1050nm~1055nm belong to B. Because from Fig. 6 one can find that there are some bumpy structure around 1050nm~1055nm when peak 1063nm 1040nm arise which is an indication that we are pumping A site. But when B site is being excited, no A site fluorescence has been observed. The fluorescence signals from A site are stronger then from B site because the signal to noise ratio is better for the former one.

At Room Temperature, we find only two sites left. Figs. 9, 10 show the emission spectra at 300K. In Fig. 9, 855.6nm and 868nm belong to A site because we are pumping with 426.98nm while 868nm and 876nm belong to B site because
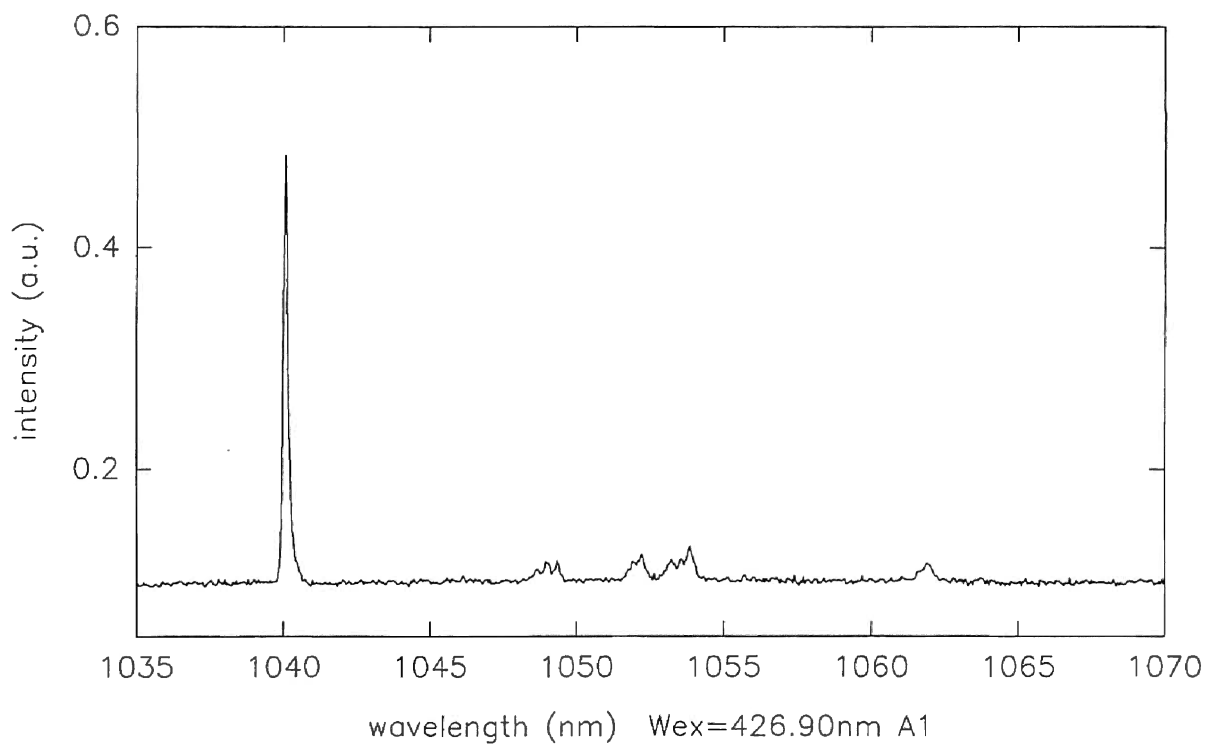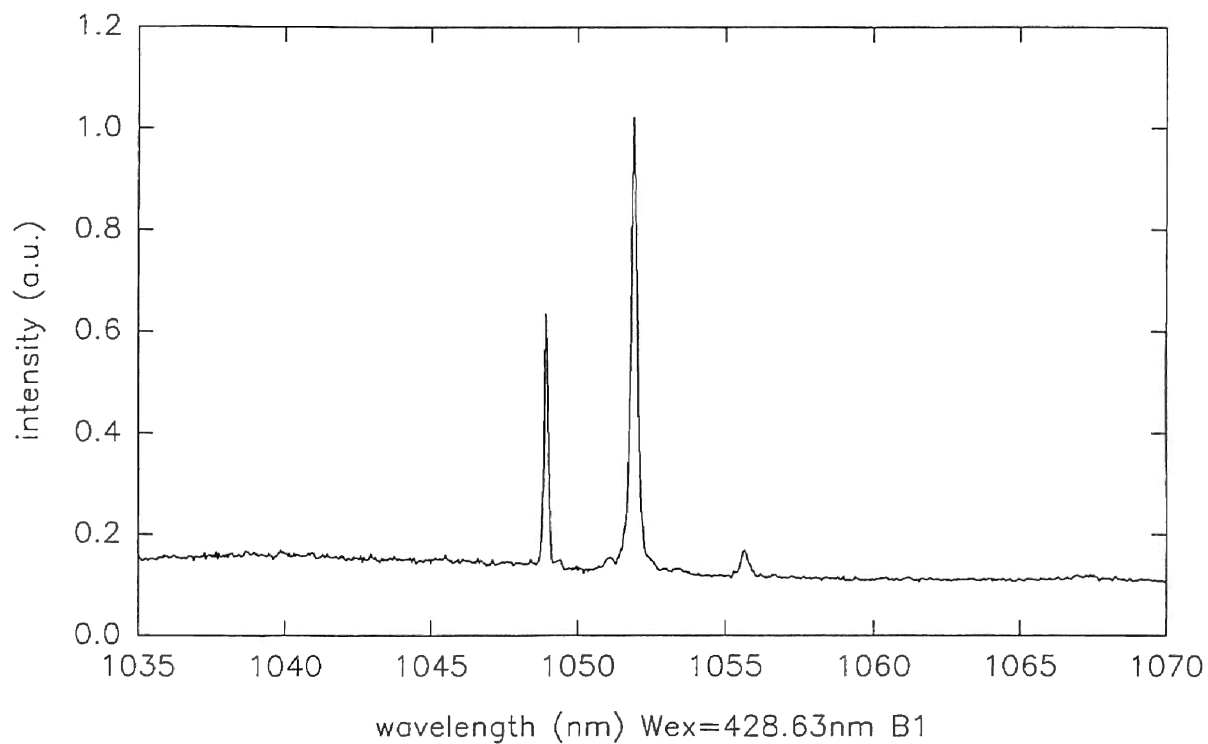
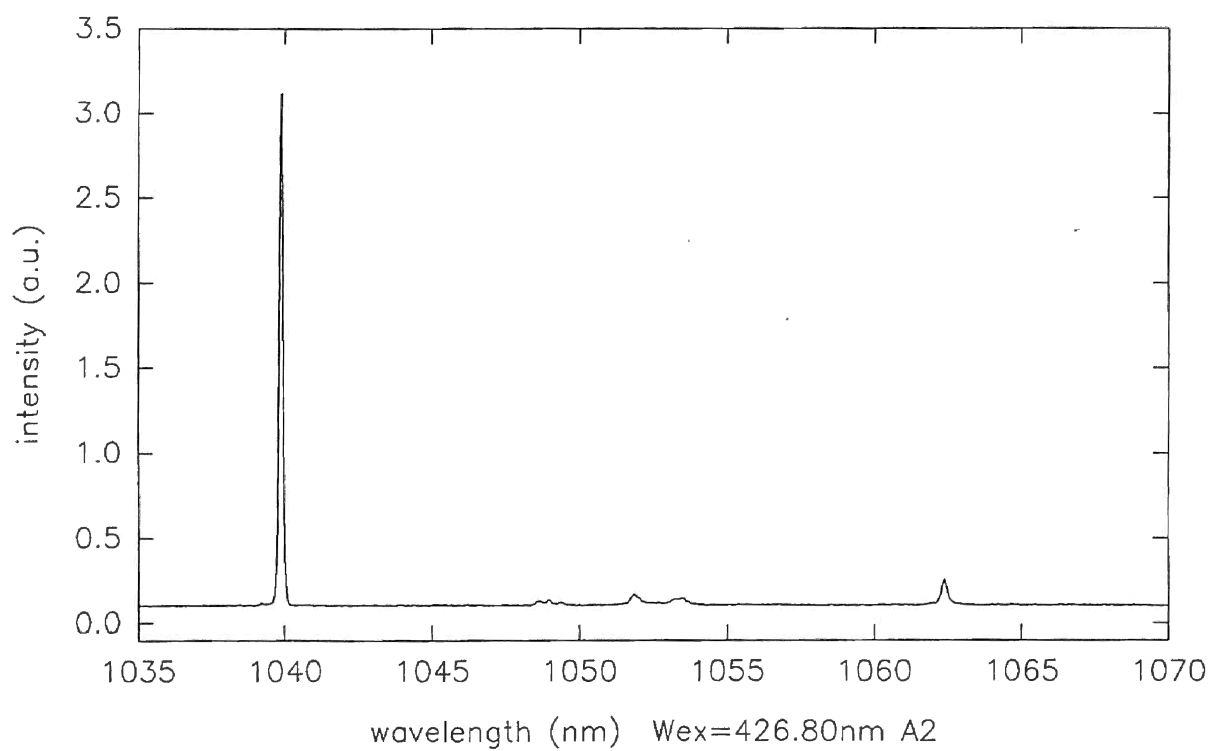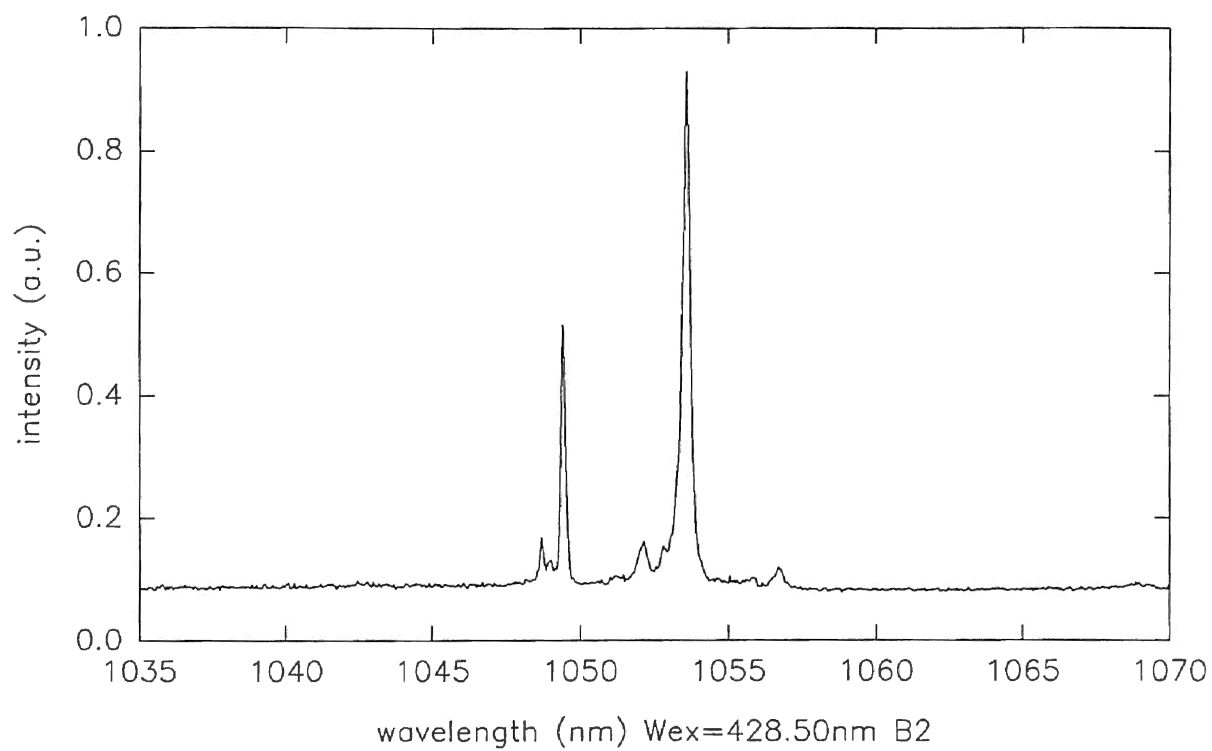Figure 6. Emission spectra at 10K. Sites B1 and A1
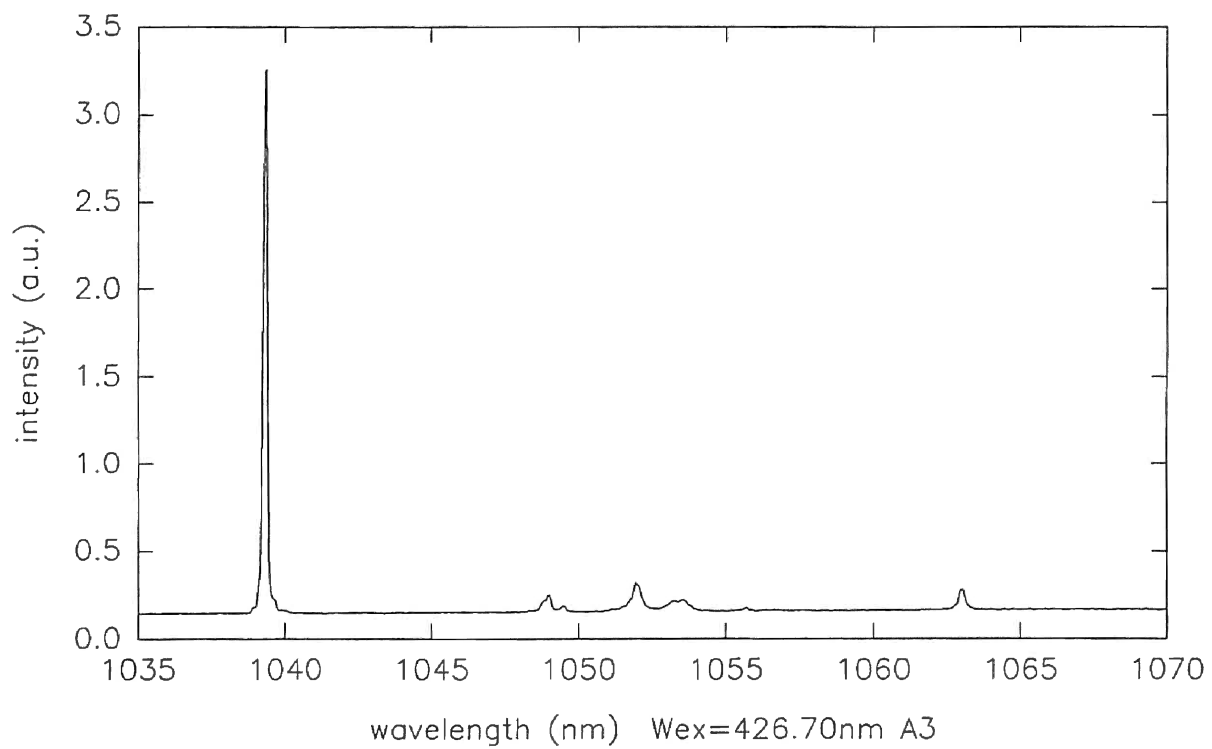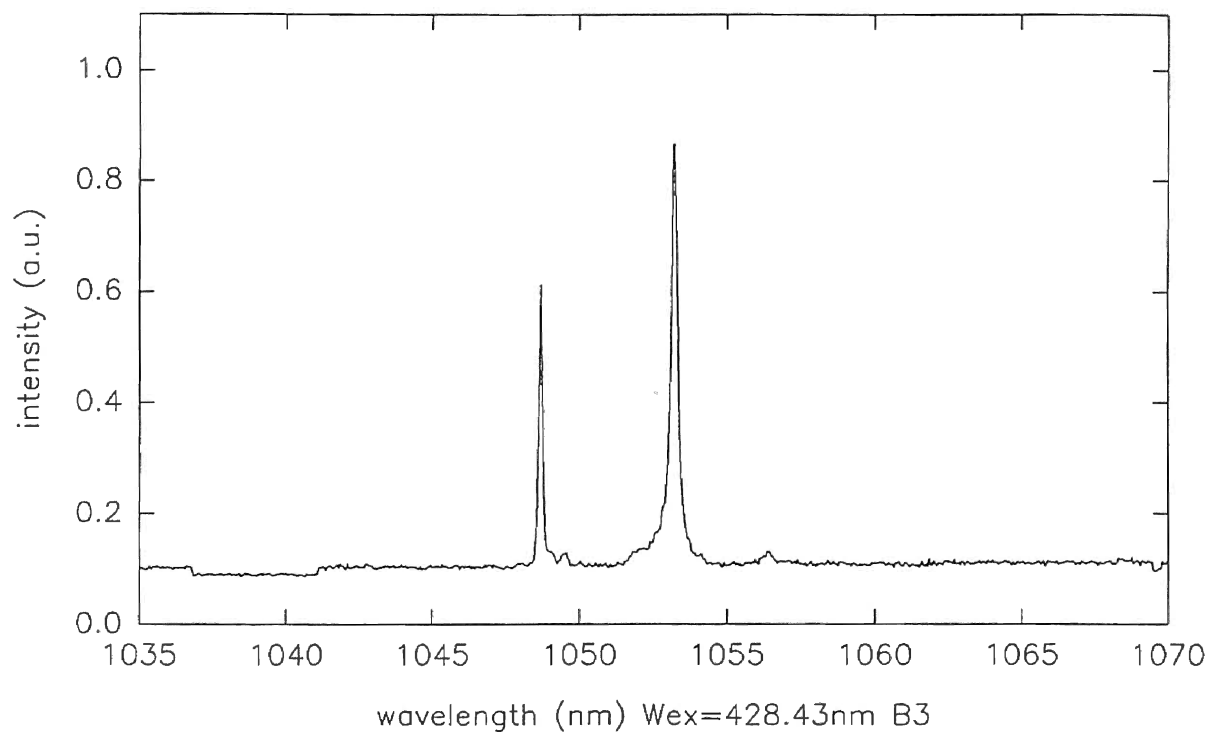
Figure 7. Emission spectra at 10K. Site B2 and A2
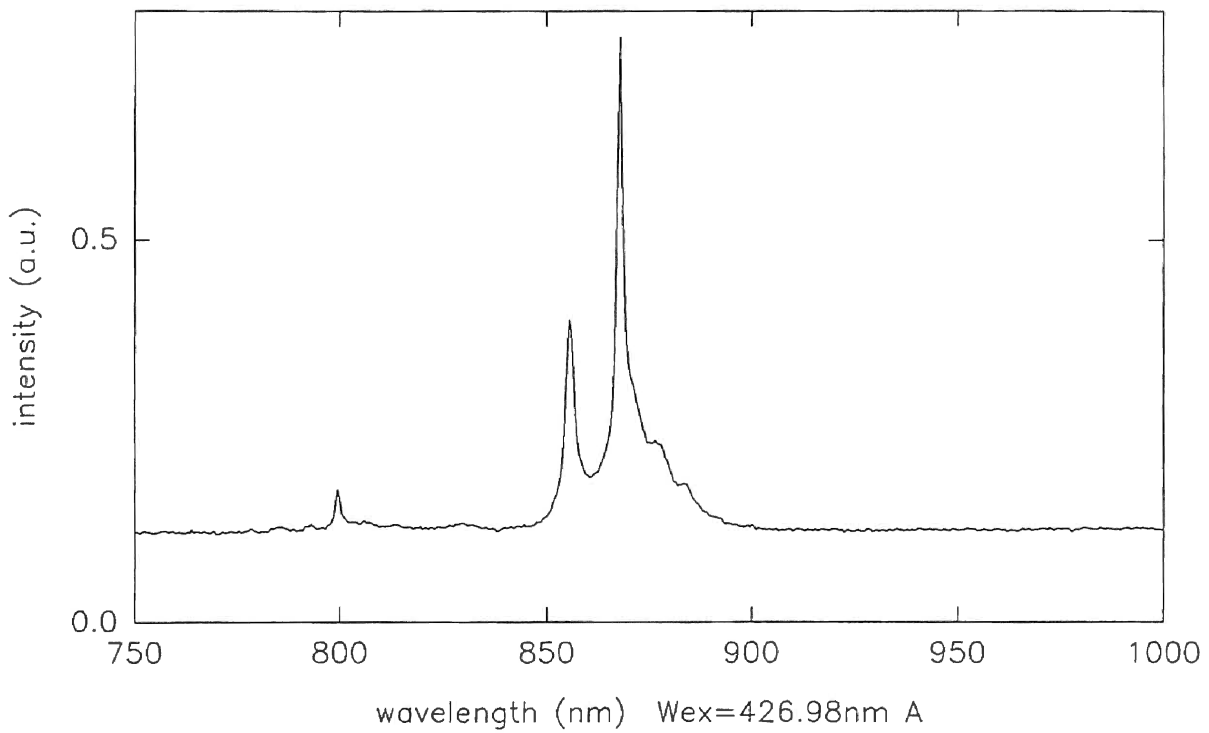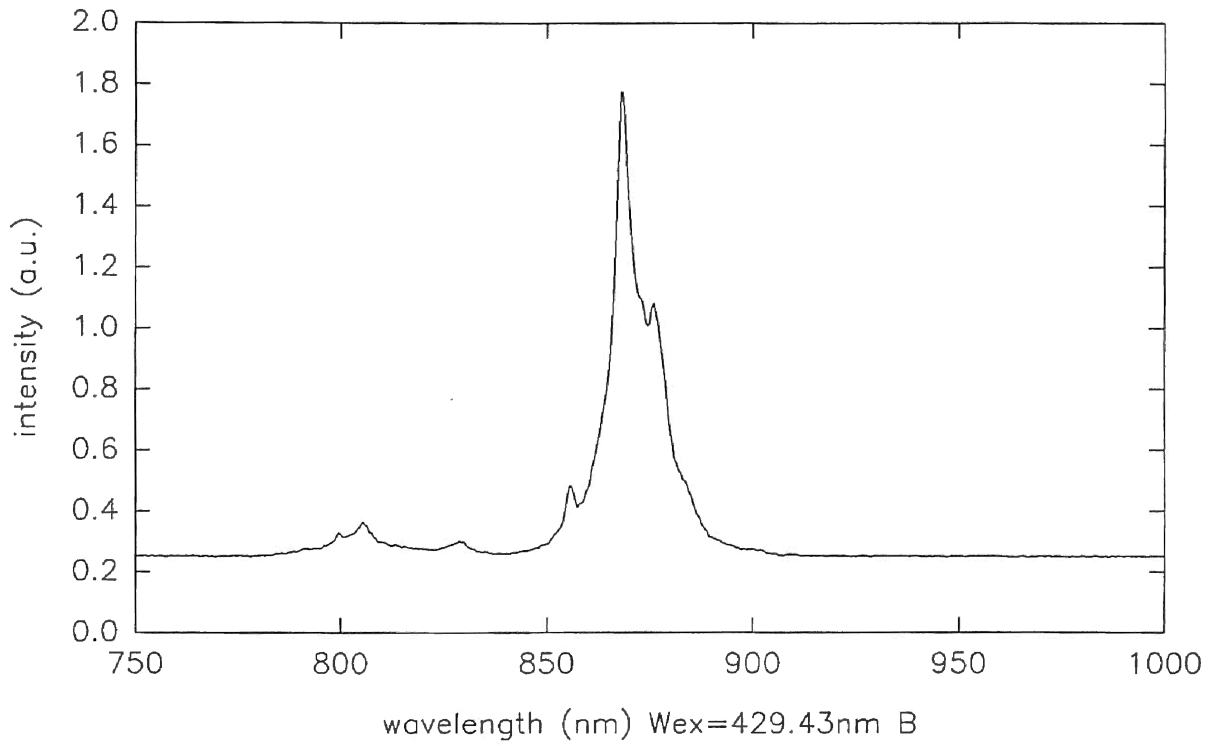
Figure 8. Emission spectra at 10K. Sites B3 and A3

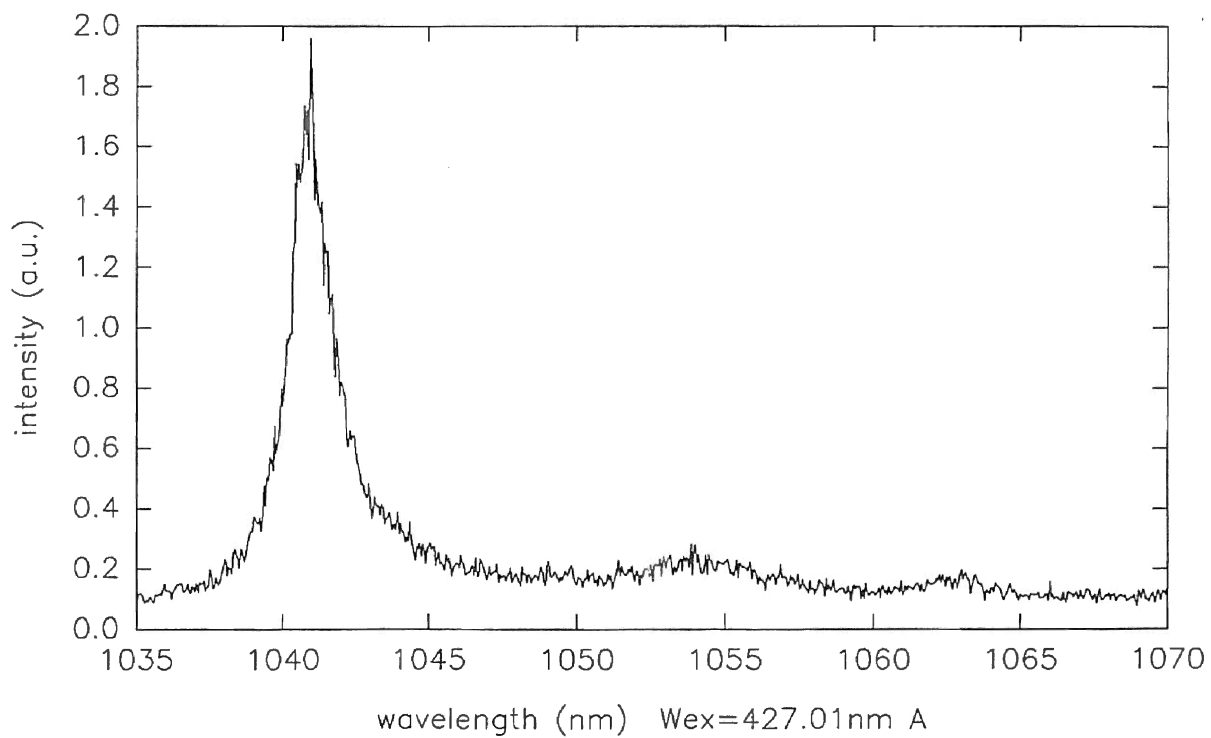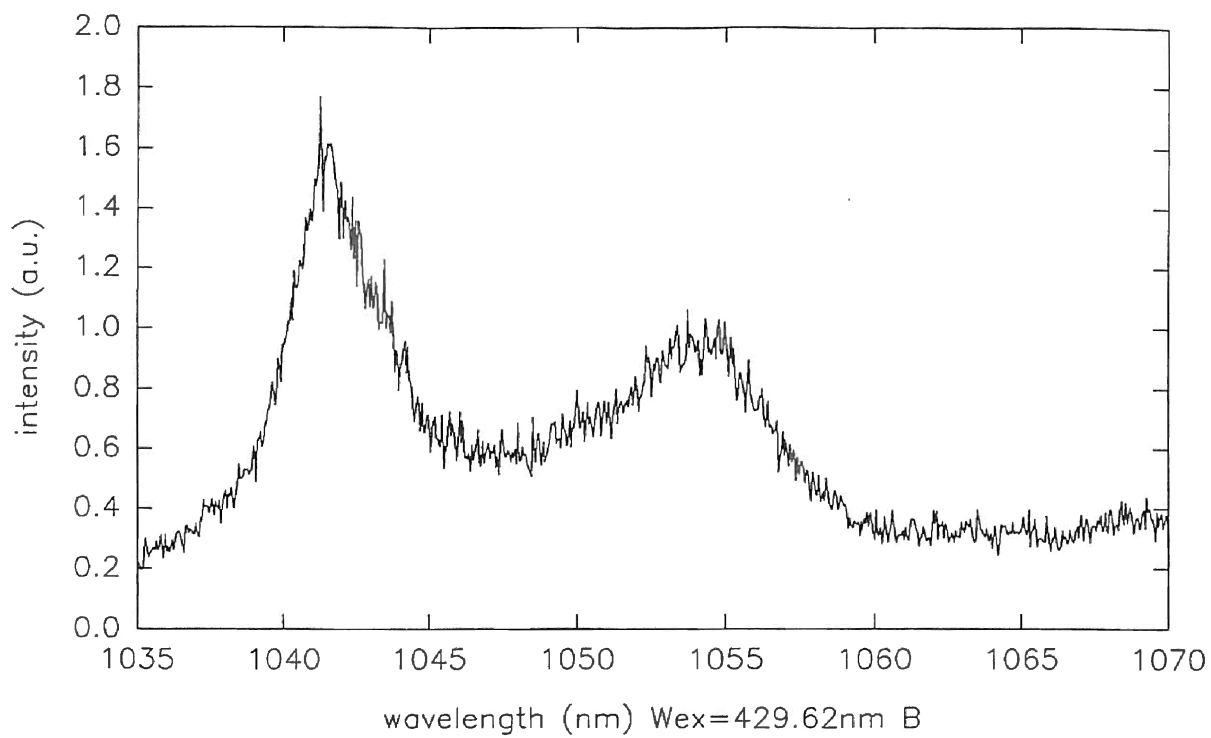Figure 9. Site A and site B emission spectra at 300K. $^4F_{3/2} \rightarrow^4 I_{9/2}$

Figure 10. Site A and site B emission spectra at 300K. $^4F_{3/2} \rightarrow ^4 I_{11/2}$

the pumping wavelength is 429.43nm. When A site is being excited, we see also B site emission and vice versa. The fluorescence from $^4F_{3/2} \rightarrow {}^4I_{9/2}$ is stronger than the transition from $^4F_{9/2} \rightarrow {}^4I_{11/2}$ by comparing the signal/noise ratio (see Figs. 9, 10). There are some other small peaks around 800nm which is the fluorescence from $^2H_{9/2} + {}^4F_{5/2} \rightarrow {}^4I_{9/2}$ (Fig. 9).

In our experiment, when we pump the atom from $^4I_{9/2}$ to $^2G_{7/2} + {}^4G_{5/2}$, we saw something different, no matter whether it's at 10K or at room temperature. The excitation wavelengths were 584.87nm to 585.85nm. We compared this position with the transmission spectrum at 10K but found no corresponding peaks. It may probably because of some other rare earth ions in the crystal like Er^{3+} which caused those emission lines.

One thing really interesting is that one can compare this result with Nd^{3+} : $LiYF_4$ [14] and Nd^{3+} : $NaYF_4$ [15]. $LiYF_4$ has a cell parameters of $A = 5.26A, C = 10.94A$ and the doped Nd^{3+} ion possesses two yttrium sites, site σ and π at 77K which depend on the polarization of the pumping wavelength. $NaYF_4$ has a unit cell parameters of $A = 5.967A, C = 3.523A$ and also has two sites , site "a" and site"f". "a" site is occupied by Y^{3+} and "f" site is occupied by $0.5Y^{3+}$ and $0.5 Na^+$. The lattice parameters for KYF_4 are $A = 14.101A, C = 10.087A$ [13]. We think the two main sites come from the replacement of Y^{3+} and K^+ by Nd^{3+} because their radii are very close, $Nd^{3+} = 0.9A$, $Y^{3+} = 0.8A$ and K^+ is 1.3A. Three subsites then may probably come from environmental change and nearest neighbors.

Room Temperature Energy Levels

By comparing our transmission spectrum with Dieke's [2] energy levels scheme of Nd^{3+} in $LaCl_3$, we determine the corresponding Nd^{3+} energy levels' position. Because although those Nd^{3+} ions are in different crystals the energy schemes are different but the corresponding position should be approximately the same.

Fig. 11 shows the results obtained by positioning the monochromator at A B site emission lines. The bottom one is the transmission spectrum of $^4I_{9/2} \rightarrow {}^4G_{7/2}$
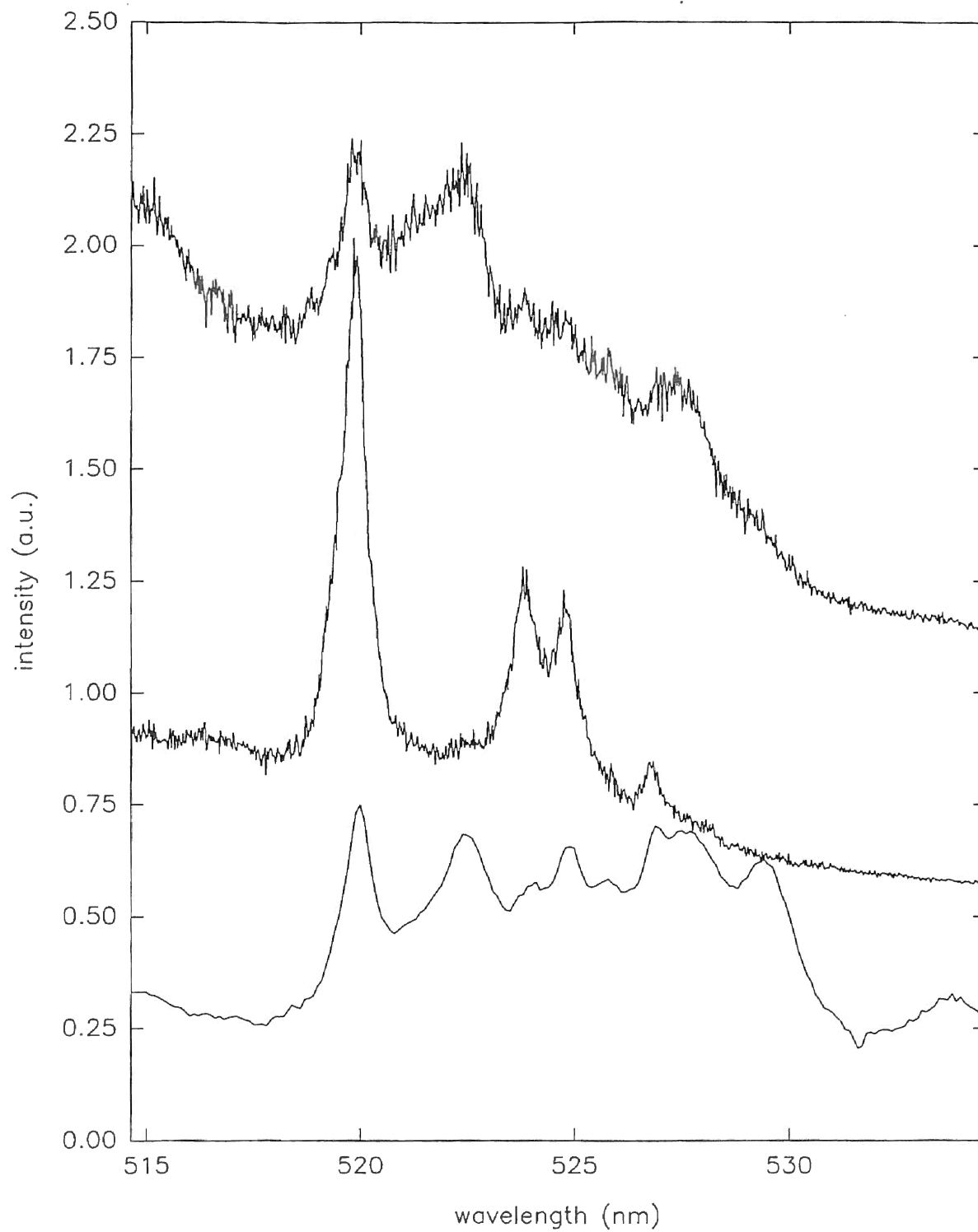
Figure 11. Position the monochrometer at A(middle one) B(upper one) sites and scan the dye laser

which is inverted in order to compare with emission spectra. The middle and the upper one are the emission spectra obtained by positioning the monochromator at 855.6nm A site and at 876.0nm B site respectively (see Fig. 9). According to the degeneracy rule, there should be $(7+1)/2 = 4$ peaks. Here we have two sites, so we expect $2 \times 4 = 8$ peaks. The dial reading on the dye laser is scanned from 25750 to 26750 for which we are using the 5th order and the dye used is Coumarine 500. The dye laser wavelength is measured by the monochromator and their position are 514.62nm and 534.58nm for dial reading $= 25750$ and 26750 respectively. Time parameter on SPEX is $0 \sim 780$sec. So we use the following formula to convert the time parameter to it's corresponding dye laser excitation wavelengths:

$$\text{wavelength scale} = 514.62nm + \frac{\text{time scale}}{780} \times (534.58 - 514.62)$$
$$= 514.62 + \text{time scale} \times 0.0259$$

Based on the relative intensities' variation, we determined the energy levels of $^4G_{7/2}$. The same method is used to determine the other energy levels. No effort is made to separate hot band transitions.

Up-Conversion Result

In this experiment, we successfully pump the atoms from $^4I_{9/2}$ to $^2G_{7/2} +^4 G_{5/2}$ and finally to R. We obtained two different kinds of emission spectra and they agree with our previous A B site result. Emission lines are observed from 350nm to 500nm, see Figs. 12, 13. Fig. 12 is A site simply because the emission spectrum from 750nm to 1000nm obtained by using the same pumping wavelength is the same as Fig. 9. Fig. 13 is assigned to be B site with the same reason. By comparing our emission spectrum with Dieke's [2] rare earth energy levels, it shows that those emissions may probably come from the transition of $^4D_{3/2} \rightarrow^4 I_{9/2}, ^4I_{11/2}, ^4I_{13/2}, ^4I_{15/2}$ or may also come from $^2P_{3/2} \rightarrow {}^4I_{13/2}, {}^4I_{9/2}$ (Fig. 14). Fluorescence life time is measured and is tabulated in Table III.

The dye laser is 10mW with a pulse width 10ns. After being focused by a 2in f $= 10$cm silica lens the minimum diameter is from Siegman [16], $f\lambda/d$:
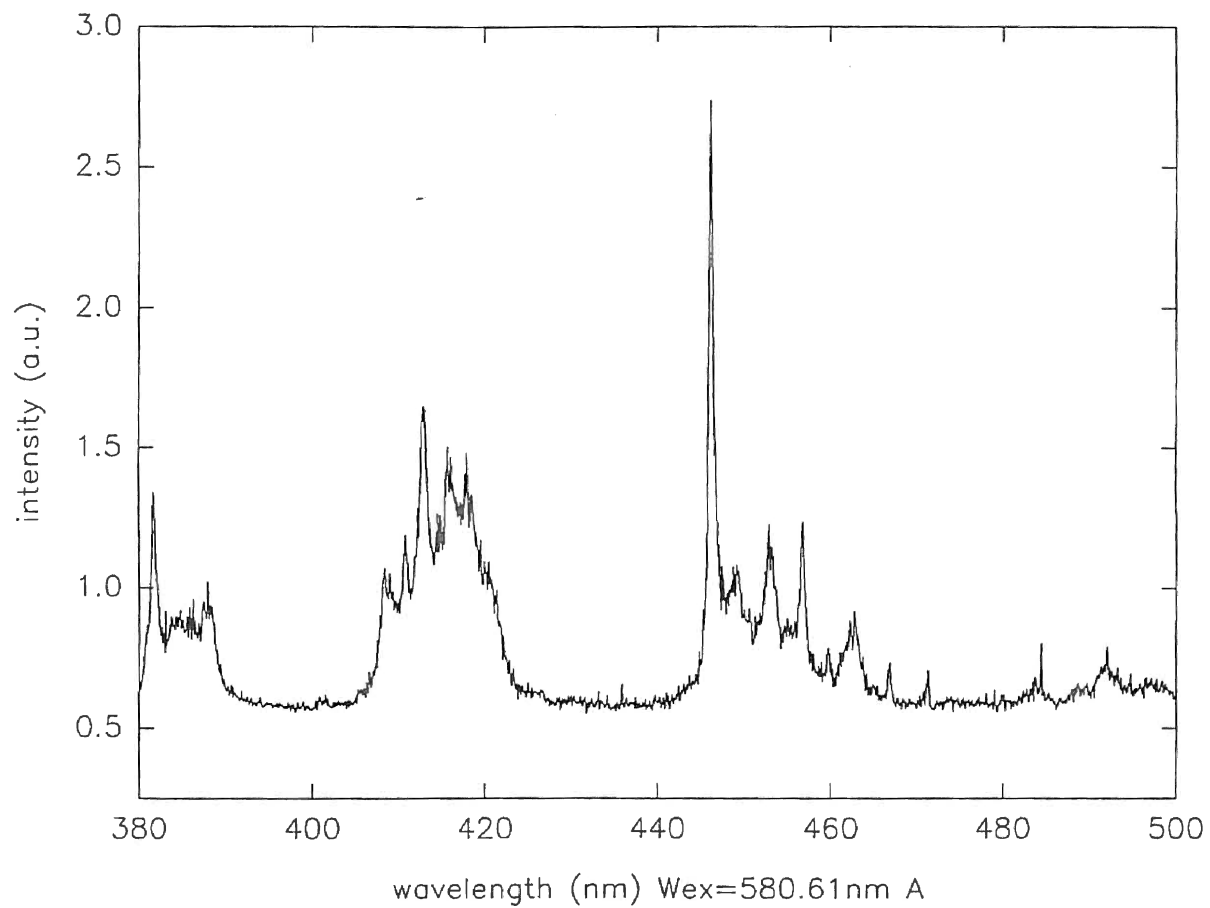
Figure 12. Upconversion blue emission. Pumping wavelength = 580.61nm, A site
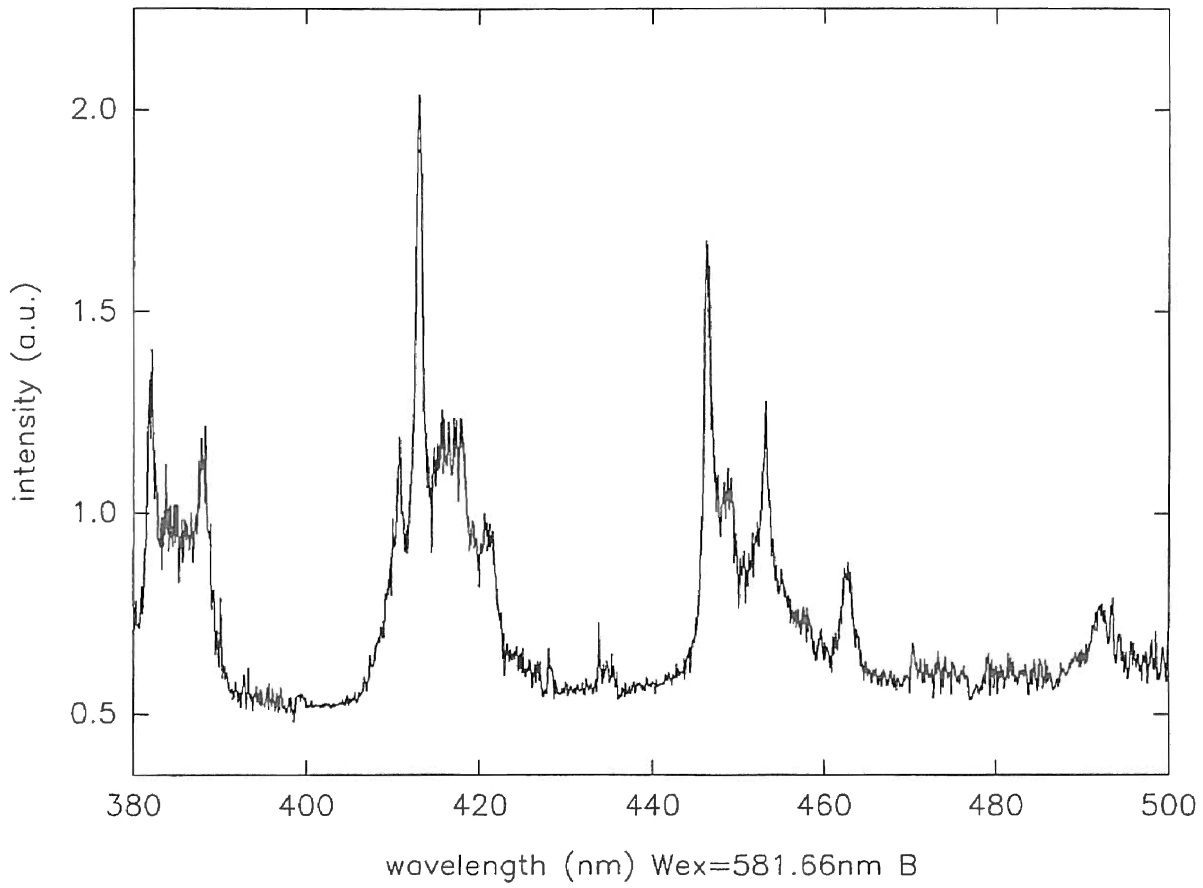
Figure 13. Upconversion blue emission. Pumping wavelength = 581.66nm. B site

$\cdot 10^3 \text{cm}^{-1}$

Energy	Level
34	R
	Q+P
32	O
30	N+M
28	$^4D_{1/2}+{}^4D_{3/2}$
26	$^2P_{3/2}$
24	$^2D_{5/2}$ $^2P_{1/2}$
22	$^4G_{11/2}$
	$^2D_{3/2}+{}^4G_{9/2}$
20	$^2G_{9/2}$ $^4G_{7/2}$
18	$^2G_{7/2}+{}^4G_{5/2}$
16	$^2H_{11/2}$
	$^4F_{9/2}$
14	$^4S_{3/2}+{}^4F_{7/2}$
	$^2H_{9/2}+{}^4F_{5/2}$
12	$^4F_{3/2}$
10	
8	
6	$^4I_{15/2}$
4	$^4I_{13/2}$
2	$^4I_{11/2}$
0	$^4I_{9/2}$

Figure 14. Possible transitions for up-conversion blue emissions

TABLE III

FLUORESCENCE DECAY LIFE TIME

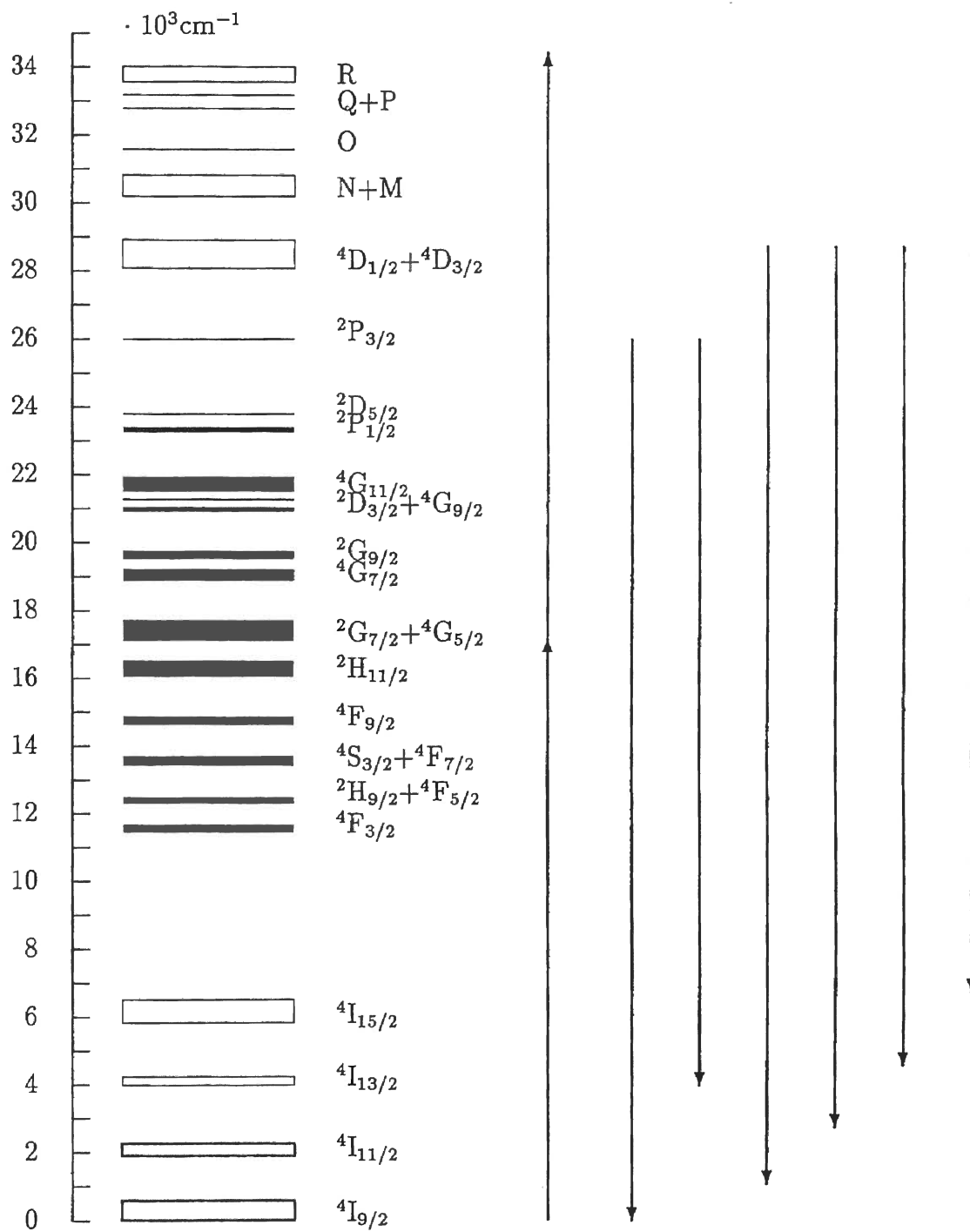| transition wavelength (nm)	decay time (μs)	site position	temperature
1048.95	844	B1	10K
1051.90	854	B1	10K
1049.30	955	B2	10K
1053.55	989	B2	10K
382.00	193	A	300K
388.00	204	B	300K
413.00	264	B	300K
446.50	268	A	300K
453.00	253	B	300K

$$d_0 = \frac{10 \times 10^{-2}m \times 580 \times 10^{-9}m}{2 \times 2.54 \times 10^{-2}m} = 1.14\mu m$$

that means the peak value of E is :

$$E_0 = \sqrt{2} \left(\frac{10^3}{2.66} \cdot \frac{0.1 \times 10^6}{\pi \times (1.4 \times 10^{-6})^2} \right)^{1/2} = 4.29 \times 10^{11} volts/cm$$

which is enough to have nonlinear effect [17].

As a result, two photon process may happen, (1) continuous absorption or, (2) absorbs two photons at the same time. More experiment need to be done to determine which process is really responsible.

Also one thing interesting is that by scanning the dye laser and position the monochromator at A B site positions we obtain two A peaks and three B peaks. Those peaks' position agree with previously determined A B site positions.

CHAPTER V

SUMMARY AND FUTURE WORK

Summary

In our site selection experiment, we obtained two main sites and each site has three subsites at 10K. At 10K, when A site is being excited, emission from B site can also be detected. But when B site is being excited, only B site emission is observed. For the transition from $^4F_{3/2} \rightarrow {}^4I_{11/2}$ at 10K, A site emission is stronger than B site emission. At room temperature, those subsites merged and only two main sites remain. The emission from $^4F_{3/2}$ to $^4I_{9/2}$ is stronger than the emission from $^4F_{3/2}$ to $^4I_{11/2}$. The fluorescence lifetime for B1 and B2 sites at 10K are $844\mu s$ and $948\mu s$.

The energy levels of Nd^{3+} ions at room temperature are determined on the basis of site selection spectroscopy result from 400nm to 880nm. Up-conversion is also obtained by pumping from the ground state to the energy level R. Emissions from $^4D_{3/2}$ to $^4I_{15/2}$, $^4I_{13/2}$, $^4I_{11/2}$, and $^4I_{9/2}$ are detected. For the up-conversion blue emission, we found there are also two sites and they agree with our previous A B sites result. The fluorescence decay times are around $250\mu s$. The strongest transition among them is the one from $^4D_{3/2}$ to $^4I_{13/2}$.

Future Work

One thing really interesting is to compare the energy levels obtained here with the theoretical calculation. The up-conversion blue emission around 350nm to 480nm suggests obtaining a blue up-conversion laser. The life time for this transition is a little too short so the efficiency of this up-conversion laser may be

low. Also, if synchronization is possible for using two dye lasers the nonradiative decay time can be measured and the energy levels of $^4I_{15/2}$ and $^4I_{13/2}$ can also be measured by utilizing the up-conversion process.

BIBLIOGRAPHY

1. A. A. Kaminskii, **Laser Crystals** (Springer-Verlag, New York, 1981).

2. G. H. Dieke, **Spectra and Energy Levels of Rare Earth Ions in Crystals** (interscience, New York, 1968).

3. M. A. Dubinskii, N. M. Khaidukov, I. G. Garipov, L. N. Dem'yanets, A. K. Noumov, V. V. Semashko, and V. A. Malyusov, Journal of Modern Optics **37**, 1355 (1990).

4. J. L. Emmet, W. F. Krupke, and J. B. Trenholme, Soviet J. quant. Electron. **10**, 5 (1983).

5. I. S. Rez, Soviet J. quant. Electron. **13**, 2071 (1986).

6. B. G. Wybourne, **Spectroscopic Properties of Rare Earths** (Interscience, New York, 1965).

7. G. Racah, Phys. Rev. **61**, 186 (1942).

8. G. Racah, Phys. Rev. **62**, 438 (1942).

9. G. Racah, Phys. Rev. **76**, 1352 (1949).

10. C. W. Nielson, and G. F. Koster, **Spectroscopic Coefficients for the p^n, d^n, and f^n Configurations** (MIT, Massachusetts, 1963).

11. E. U. Condon & Shortly, **The Theory of Atomic Spectra** (Cambridge, London, 1951).

12. B. R. Judd, Operator Techniques in Atomic Spectroscopy (McGraw-Hill, New York, 1963).

13. Aleonard S, Le Fur Y, Pontonnier L, Gorius N F, and Roux M Th, Ann. Chim. Fr. **3**, 8959 (1991).

14. A. L. Harmer, A. Linz, and D. R. Gabbe, J. Phys. Chem. Solids **30**,1483(1969).

15. M. F. Joubert, C. Linarès, and B. Jacquier, J. Lumin. **51**, 175(1992).

16. A. E. Siegman, **Lasers** (University Science Books, California, 1986).

17. J. A. Armstrong, N. Bloembergen, J. Duching, and P. S. Pershan, Phys. Rev. **127**, 1918 (1962).

VITA

LIANG-CHIUN CHAO

Candidate for the Degree of

Master of Science

Thesis: SITE SELECTION AND LASER SPECTROSCOPY OF ND^{3+} IN KYF$_4$

Major Field: Physics

Biographical:

Personal Data: Born in Taichung, Taiwan, R. O. C., October 19, 1967, the son of Wei-Chiang CHAO and Yu-Lin PAO.

Education: Received Bachelor of Science Degree in Physics from Fu-Jen Catholic University, Taipei, Taiwan, R. O. C.,1989, completed the requirement of Master of Science at Oklahoma State University, Stillwater, Oklahoma in July, 1993.